Role of Short Chain Branching in Crystalline Model Polyethylenes

William Fall, Jörg Baschnagel, Olivier Lhost, Hendrik Meyer

The Role of Short Chain Branching in Crystalline Model Polyethylenes

William S. Fall,*,† Jörg Baschnagel,† Olivier Lhost,‡ and Hendrik Meyer*,†

†*Institut Charles Sadron, Université de Strasbourg & CNRS, 23 rue du Loess, 67034 Strasbourg Cedex, France.*

‡*Total Research & Technology Feluy, Zone Industrielle Feluy C, B-7181 Seneffe, Belgium.*

E-mail: william.fall@ics-cnrs.unistra.fr; hendrik.meyer@ics-cnrs.unistra.fr

Abstract

The role of short chain branches (SCBs) (C_4H_9) on the melt and crystalline properties of monodisperse polyethylene systems ($C_{400}H_{802}$) is investigated, using molecular dynamics simulations of a coarse-grained united-monomer model that represents a chemical monomer as one particle. A method is introduced, whereby SCBs are grown out of the linear backbone to minimise computational expense. Here this concept is proven by introducing differing numbers (N_b = 0, 1, 2, 4, 10 and 20) of regularly-spaced SCBs along the chain backbones and studying their influence on the melt and crystalline properties. By growing SCBs into the melt phase, it is demonstrated that they marginally perturb the original topology, justifying a relatively short equilibration time after growth. Upon crystallisation however each system's behaviour differs considerably. Cooling and heating cycles are performed to study crystallisation and melting at progressively slower rates. The crystalline morphology is observed to depend strongly on both cooling rate and number of branches along the linear backbone. In particular, the lamella thickness decreases systematically with both faster cooling and increasing SCB content. At the highest branch content, of one per 20 backbone

carbons ($N_b = 20$), crystallisation is almost entirely suppressed whereas a small number of branches allows control over the average lamellar thickness. This observation, combined with a prudent method for equilibrating systems with SCBs, opens up opportunities to study more complex chain architectures and mimick industrial polyethylene morphologies.

Introduction

Polyethylene (PE) as a linear hydrocarbon chain is the most simple polymer one can think of. Due to its regular structure, it crystallizes easily. Long alkanes up to C_{192} are known to form extended chain crystals,[1] and longer polymers generally form semi-crystalline structures consisting of chain-folded crystalline lamellae separated by disordered interphases.[2] However, the mechanical properties of these PE solids are rather poor as the crystal planes can slide against each other under weak or moderate deformation. Simulations suggest that entanglements are shifted to the interphase region upon crystallization[3] and that this enhanced entanglement density correlates with the stress-strain behavior of the polymer.[2] Changes of the interphase properties, created by molecular architecture such as chain branching, can therefore be expected to impact the mechanical behavior of PE. For instance, it is known that mechanical properties like the compromise between material rigidity and impact resistance are highly dependent on the content of short chain branches (SCBs) and long chain branches (LCBs) of PE. The unique properties of linear low density polyethylene (LLDPE), such as high flexibility and tear-resistance for example, originate from the introduction of short chain branches placed along the backbone,[4] a few per thousand carbons are sufficient to change properties. Fundamental studies of polymer crystallisation, i.e. the effect of short chain branching and supercooling on crystal growth rate, final polymer morphology and material properties are however challenging. The primary reason for this is the issue of polydispersity. In a polydisperse system there is a distribution of chain lengths and the wider the distribution the more the regularity of the chain folded structures is destroyed.

This is owing to the incomplete traverse of chains of unequal lengths between layers of a single crystalline lamella, which both lowers the final crystallinity and generally prevents the formation of perfect crystals, where chain ends might have otherwise crystallised at the lamella surface. One solution to this problem is to work with a narrow molecular weight distribution or better still monodisperse systems of n-alkanes where fundamental questions can be tackled more precisely.

Crystalline n-alkanes, long enough to form chain folded structures with SCBs, have been studied widely as model chain molecules.[1,5–10] Zeng et al carried out a series of such studies on both symmetrically branched and asymmetrically branched n-alkane systems. They report the so-called F2 form, non-integer fold (NIF) and mixed folded extended (FE) forms, which forms a 3-layer superlattice in the case of symmetrical branches. Note the F2 form appears first and transitions to NIF on cooling either from the melt or solution. Further double-layer and triple-layer crystalline forms can be found in asymmetrically branched systems on cooling from two different semi-crystalline forms at high and low crystallisation temperature (T_c) respectively. At high T_c it was found that the longer arm at the asymmetrical branch point crystallises as an extended chain with the shorter arm remaining in the amorphous region; the opposite scenario occurs at lower T_c. This leads to two different, double or triple-layer, crystalline structures on further cooling. Further Y-shaped n-alkanes stars with two long arms and one short arm were also investigated and a further semi-crystalline form discovered where the long arms either once-fold and crystallise with the shorter arms rejected into the amorphous region or only a single long arm may crystallise where one short and one long arm remain in the amorphous region. On further cooling this transitions to a double layer superstructure with one thick layer of extended long arms and a short layer of once-folded long and extended short arms. Such conclusions however may only be reached from arguments hinging on the extent of amorphous fractions and thickness of lamellar regions and are inferred as opposed to directly observed. These studies allow for general conclusions to be drawn for example, the number of chains crossing the crystal-amorphous interface,

equilibrium and kinetic crowding effects, fold adjacency etc. Whilst these experiments reveal much about polymer crystallisation, they cannot resolve the dynamics of individual polymer chains during the nucleation stage or as a polymer crystal is growing and chains adsorb, desorb and resorb at the crystal front. Nor can purely monodisperse n-alkanes in excess of 390 carbons be studied, which is to date the longest ever purely monodisperse n-alkane ever synthesized.[11] Molecular dynamics simulations can however monitor such behaviour in real time and shed light on open questions on the subject,[12] providing a rigorous test of competing theories of polymer crystallisation.[13]

To that end, we propose a new united-monomer model to examine how sensitive the crystallization behavior is to the presence of a few short chain branches in classical molecular dynamics simulations. Due to its simple structure, PE has been studied with molecular dynamics since the first days of polymer simulations. A recent review gives an overview on experimental properties which have been simulated with united-atom models.[2] United-atom (UA) models absorb hydrogens with the heavy atom they are connected to.[12] This strongly reduces the complexity of simulation because of the reduction of particles, and the reduction of intra-chain angular and torsional potentials. UA models have been very successful in calculating melt properties. However, with the removal of explicit hydrogens, UA models are not able to form the orthorhombic unit cell of PE crystals.[14] Nonetheless, UA models of polyethylene have been frequently used to study aspects of polymer crystallization.[2,4,15,16]

Unfortunately, one needs very big simulation boxes to study the interaction of many crystal domains – the typical thickness of semi-crystalline lamellae is in the order of 10 nm. Such large systems currently cannot be addressed by atomistically detailed simulations. Assuming, however, that the large scale distribution of crystalline and amorphous interphase regions is dominating the mechanical properties, it may be not important to realistically reproduce the local crystal structure. This leads us to employ a united-monomer model adapted for PE. 20 years ago, a united-monomer model derived for poly-vinyl alcohol (PVA) demonstrated for the first time that the formation of semi-crystalline structures can be obtained

via MD simulations from the quiescent melt.[17,18] It has been shown that the repulsive part of the potential, together with an angular potential obtained from Boltzmann inversion,[19] is enough to trigger the crystallization and that the trend of lamellar thickness as a function of crystallization temperature was realistic. The CG-PVA model has been further used by other groups.[20,21] When modified with an attractive part of the potential, it has been used recently to study deformation of semi-crystalline polymers.[22,23] Note that other groups have come up recently with more coarse-grained models which show also the ability to form semi-crystalline structures.[24,25] When studying melt properties, it is common to employ higher levels of coarse-graining[26–28] with more than two carbons per CG bead. Where the study of phase transitions is concerned however, we believe that a CG unit representing more than two carbons is too far removed from the real polymer, this results in many important chain conformations being coarse-grained out and makes it challenging to relate results to the real polymer. It is important to note that, in general, a coarse-grained force field is only precise at the state point where it has been parameterized. The range of validity can be significantly improved if several state points are included in the coarse-graining procedure.[29] The transferability across phase transitions is still more complex, espcecially with highly ordered phases where some conformations are excluded. The mapping must thus be performed in the melt where all conformational states are accessible. Therefore, following the success of the CG-PVA model in simulating polymer crystallization, we here determine the force-field of PE in the melt and then make the approximation that the same force-field may be used at all temperatures.[17]

We choose to use a united monomer approach similar to previous works[17,30] since it facilitates a significant speed-up with respect to united-atom models, while still having a well-defined mapping of angular states as outlined in the proceeding section. Next, a method is described whereby SCBs may be grown into the monodisperse linear melt, which is advantageous in large systems of long chains where equilibrium times are long and prove the concept by examining the melt properties usually used to characterise well equilibrated polymer

melts. Then we report the results of continuous cooling and heating cycles, on the crystallisation and melting behaviour of systems comprising different numbers of SCBs, for a series of cooling and heating rates. Finally we conclude and compare our results to the relatively few other simulation studies involving SCBs that have been performed to date[4,14,24,31–38] noting some important trends and highlighting future questions to be addressed in a forthcoming study.

Methods

United-Monomer Model

An adaption of the united-monomer model of poly-vinyl alcohol, originally outlined in,[17,39] is presented here for polyethylene. In the united-monomer model a single coarse-grained (CG) bead corresponds to an ethylene monomer, i.e. to two CH_2 groups, as depicted in Fig. 1. Most coarse-graining procedures choose the center of mass of the group of atoms contained in one CG bead as the mapping point.[26,27] In contrast to this, we use every second carbon as the mapping point to determine the CG distributions.[40] As already outlined by Reith et al.,[19] this avoids cross-correlations between angles and bonds for low coarse-grained levels and preserves a direct interpretation of the angular potential. As a result, the CG bond can be modelled by a harmonic potential of the form,

$$U_{\text{bond}}(l) = \frac{1}{2} k_{\text{bond}} (l - l_0)^2 \tag{1}$$

where U_{bond} denotes the potential energy change associated with a deviation in bond length l from its equilibrium value l_0 and k_{bond} is the spring constant as defined in Tbl. 1. For details of the all atom reference simulations and how these parameters are obtained please see Supporting Information.

The distinguishing feature of the united-monomer model for PE is its characteristic an-

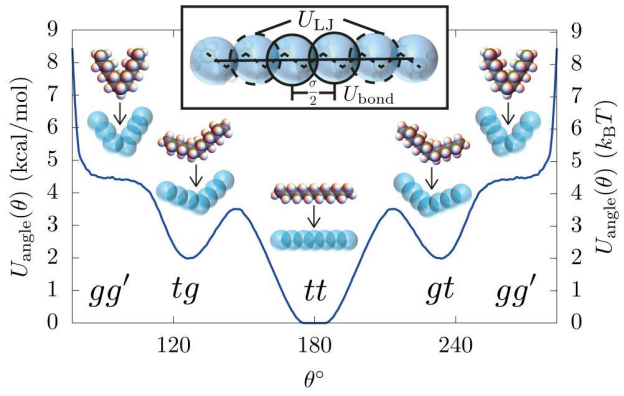

Figure 1: Schematic representation of the coarse-grained model for PE, (blue) beads represent two CH_2 groups, where non-bonded interactions and bonded interactions are indicated, with the equilibrium bead separation $l_0 = \sigma/2$. Mapping from an all atom torsional potential to CG tabulated angular potential. The three minima correspond to gauche-gauche (gg'), trans-gauche (tg) and trans-trans (tt) conformers in the all atom representation of PE as depicted in the inset artistic representations.

gular potential, obtained via Boltzmann inversion from fully atomistic simulations.[30] In this procedure the bond angle probability distribution $P(\theta)$, obtained via all atom simulations, is inverted to produce a bending potential $U_{\rm angle}(\theta) = -k_{\rm B}T \ln[P(\theta)/\sin\theta]$. The torsional potentials in the all atom representation of PE are effectively coarse-grained out into a unique tabulated angular potential between three successive beads as shown in Fig. 1. This represents the potential energy change associated with deforming the angle from the equilibrium *trans-trans* configuration at 180°. In this way the bending potential preserves a clear interpretation of the conformational restrictions associated with the fully-atomistic torsional states (hindered rotations) of PE as indicated by the arrows in Fig. 1 for the *gauche-gauche*, *trans-gauche* and *trans-trans* states, respectively.

Table 1: Parameter value for the united-monomer model of PE in Lennard-Jones and real units, where $\sigma = 0.5$ nm is the size of one CG-PE bead and $T_0 = 227$°C is the reference temperature of the melt.

Unit	$k_{\rm bond}$	l_0	σ_0	ϵ_0
Reduced	1350 ($k_{\rm B}T_0/\sigma^2$)	0.5 (σ)	0.89 (σ)	0.37775 ($k_{\rm B}T_0$)
Real	53.69 (kcal/mol/Å^2)	2.225 (Å)	4.45 (Å)	0.348 (kcal/mol)

Intra-molecular non-bonded interactions between beads, separated by three or more successive bonds, and inter-molecular non-bonded interactions are described by a soft pairwise 9-6 Lennard-Jones (LJ) potential as follows,

$$U_{\mathrm{LJ}_{9-6}} = 4\epsilon_0 \left[\left(\frac{\sigma_0}{r}\right)^9 - \left(\frac{\sigma_0}{r}\right)^6 \right], \quad r \leq r_\mathrm{c} \tag{2}$$

where ϵ_0 denotes the depth of the potential well, σ_0 the zero-crossing (particle size) as defined in Tbl. 1, r the inter-particle separation and r_c the cutoff distance. The potential is cut and shifted to zero at the minimum $r_\mathrm{c} = 1.02\sigma$ ensuring only repulsive interactions. While investigation of the stress-strain behavior upon deformation requires the inclusion of the attractive part of the potential,[22,23] it has previously been shown that a purely repulsive potential is sufficient for studies of quiescent systems.[17,18,20,21] Therefore, we adopt this approach here. Electrostatics are not explicitly taken into account in this model as a monomer has no net charge. The 9-6 potential has been chosen because the united monomer has an effective interaction which is softer than a standard 12-6 LJ potential.[19] Note that more precise potentials could be obtained at specific state points by iterative Boltzmann inversion using tabulated potentials.[27,32,41]

The initial PE melt comprised of either $M = 384$ chains for $N_\mathrm{b} \leq 1$ or $M = 768$ chains for $N_\mathrm{b} > 1$ (with N_b denoting the number of SCBs), where each chain has length $N = 200$ ($\mathrm{C}_{400}\mathrm{H}_{802}$). This is prepared via enumeration of an ensemble of M freely rotating chains such that the characteristic ratio corresponds to the expected chain dimension. Next, a slow push off method is used to remove inter-chain overlaps via a force-capped potential which is gradually increased to the full LJ potential.[42] This step is performed in the canonical NVT ensemble with a homemade molecular dynamics (MD) simulation code. All further equilibration and production runs are then performed using the Large-Scale Atomic/Molecular Massively Parallel Simulator (LAMMPS).[43,44] The disordered melt is subject to equilibration runs in the NPT ensemble at constant pressure P via a Langevin thermostat, with coupling

constant $\Gamma = 0.5$ $(1/\tau)$ and a Berendsen barostat with $P_{\rm damp} = 100.0$ (τ). We always use the integration timestep 0.005 τ, where the LJ-time unit $\tau = \sqrt{m\sigma^2/k_{\rm B}T_0}$ corresponds to 2.7 ps ($m = 27.3881$ g/mol) and temperature is held fixed at $T_0 = 500$ K = 227°C ($T = 1.0$ in reduced units). Note that while length scales are quite exactly mapped, the time conversion is very approximate because the free energy landscape of CG models is much smoother. To compensate for the absence of attractive non-bonded forces, a high pressure $P = 8.0$ $(k_{\rm B}T_0/\sigma^3)$ is applied to obtain the desired density. After equilibration, we switch to a Nosé-Hoover thermostat and barostat for all production and cooling runs with $T_{\rm damp} = 2.0$ (τ) and $P_{\rm damp} = 100.0$ (τ) respectively.

Short Chain Branching

The procedure for introducing short chain (Butyl) branches (SCBs) into the monodisperse PE systems considered in this work, with $N_{\rm b} = 0$, 1, 2, 4, 10 and 20 branches, proceeds as follows. First the backbone position corresponding to the regular spacing $p_i = (i+1/2)N/N_{\rm b}$, where $i = 1, ..., N_{\rm b}$, is copied and shifted normal to the chain backbone by half the bond length as shown in Fig. 2. This is then followed by the remaining beads along the branch such that the new beads all lie along the vector normal to the chain backbone with spacing $\sigma/4$ ensuring there are no direct overlaps, as depicted in Fig 2(a). Butyl corresponds to two coarse-grained beads in the united-monomer model.

After the topology has been modified, the newly inserted beads are pushed out into the melt, according to the procedure depicted in Fig. 2(a-d), using hybrid pair styles. Non-bonded interactions between backbone atoms (AA) take place via the standard LJ potential in Eqn. (2) at full strength, according to the values given in Tbl. 1. All other interactions (AB and BB) use a soft non-diverging potential of the form,

$$U_{\rm soft}(r) = A\left[1 + \cos\left(\frac{\pi r}{r_{\rm c}}\right)\right], \quad r \leq r_{\rm c} \tag{3}$$

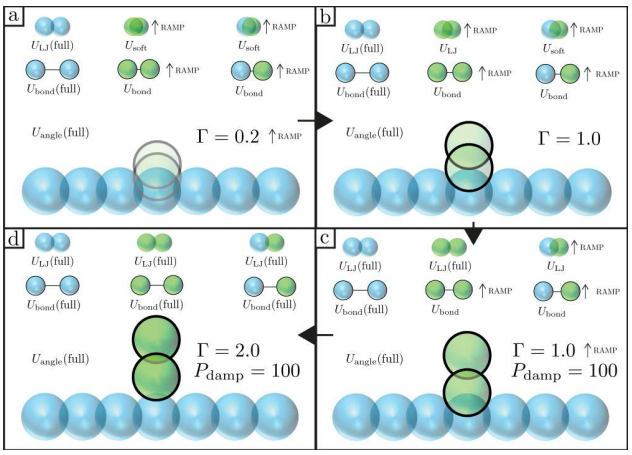

Figure 2: (a-d) Protocol for the insertion of branches along the chain backbone and growth into the melt phase. Blue and green beads correspond to backbone (species A) and branch beads (species B), respectively. The inset illustrations are representative of the gradual ramping of model parameters, Γ and P_{damp} indicate changes to the friction coefficient of the Langevin thermostat and introduction of a Berendsen barostat. For precise timings, a sample LAMMPS script can be found in Supporting Information.

where A is the amplitude at $r = 0$ and r_{c} is identical to the cutoff radius defined previously. The non-bonded interactions for species B are increased rapidly over a short timescale, followed more slowly by cross-species interactions (AB) and bonded interactions for species B. This is shown in Fig. 2(a) and is performed until the distances between beads becomes sufficiently large to ensure switching to the U_{LJ} potential does not destabilise the system. During this phase of the procedure a Langevin thermostat is used with a stronger the friction coefficient. For precise values see the sample LAMMPS script in Supporting Information.

Once this initial growth stage is complete, the non-bonded interactions between species B are switched from U_{soft} to U_{LJ} with softer coefficients and the friction coefficient of the Langevin thermostat is reduced as depicted in Fig. 2(b). At this stage only the cross-species interactions take place via U_{soft}. The non-bonded interactions for species B are then raised rapidly to their full values, followed more slowly by the bonded interactions, at which point the cross-species interactions are then switched from U_{soft} to U_{LJ}. The cross-species interactions are quickly raised to their full values alongside and bonded interactions for species B as shown in Fig. 2(c-d), to approximately half the full stiffness. Next, a Berendsen

barostat is introduced and the bonded interactions for species B are rapidly brought to their full values. The friction coefficient of the Langevin thermostat is then set to its final value and a short equlibration run, in comparison to the monodisperse systems with SCBs, is performed.

All systems considered in this work, including the initial linear configuration into which branches are grown, are then subjected to isothermal equilibration runs at 227°C (500 K) for 500×10^6 timesteps ($\sim 6.7\ \mu s$) using a Langevin thermostat and Berendsen barostat. Note that similar runs with a Nosé-Hoover thermostat and barostat yield identical results. The systems with SCBs are equlilibrated further in order to demonstrate how the addition of short branches, into a fully relaxed linear PE melt, can be considered as a small perturbation. In this way a short isothermal run, after SCBs are grown into the linear melt, may be justified. This method is particularly useful for simulations of very large systems, where computations are expensive, and is employed as a cost saving measure in a forthcoming paper. In the following section, the structural characteristics of single chains in the melt are briefly discussed and compared to theoretical predictions.[45–47]

Melt Properties

Polymer stiffness may be determined by its characteristic ratio (C_∞)[46] which can be defined as

$$C_\infty = \lim_{s\to\infty} C(s)\,, \quad C(s) = \frac{\langle R^2(s)\rangle}{s\langle l^2_{\mathrm{CH}}\rangle} \tag{4}$$

where $\langle R^2(s)\rangle$ is mean-square internal distance (MSID) between a given monomer and the s-th neighbour along the backbone in number of bonds and $\langle l^2_{\mathrm{CH}}\rangle$ the mean-square length of chemical bond (i.e. of the atomistic chain model). For the CG-PE model studied here, the

MSID may be accessed via

$$\langle R^2(s)\rangle = \frac{1}{M}\frac{1}{N-s}\sum_{i=1}^{M}\sum_{j=1}^{N-s}\left\langle(\mathbf{r}_{i,j}-\mathbf{r}_{i,j+s})^2\right\rangle \tag{5}$$

where $\mathbf{r}_{i,j}$ is the position of the j-th bead in the i-th chain, s is the curvilinear distance between beads j and $(j+s)$ along the chain backbone in number of bonds, the sums run over all possible bead pairs $(N-s)$ and all chains M, and $\langle\ldots\rangle$ means the average over the time series of configurations. The MSID has been used extensively in previous simulation studies to evaluate the degree of relaxation in long-chain polymer systems and to study conformational polymer properties.[23,42,48–50]

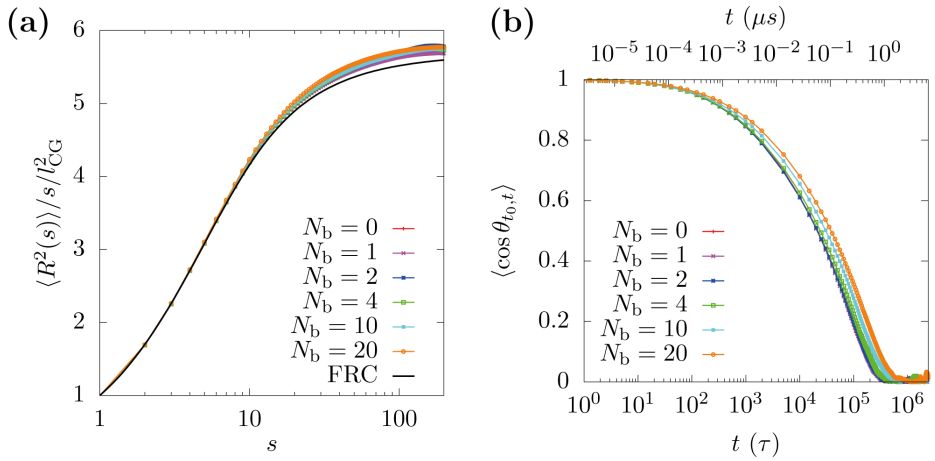

Figure 3: (a) Comparison of the mean-square internal distance $\langle R^2(s)\rangle/s\langle l_{CG}^2\rangle$ as a function of curvilinear distance s along the chain backbone for CG-PE systems with $N_b = 0$, 1, 2, 4, 10 and 20 branches. The predicted MSID from the freely rotating chain (FRC) model is indicated by the solid line for $\alpha = -\langle\cos\theta\rangle = 0.7003$, cf. Eqn. (6). The 'tetris-like' schematics indicate the colour correspondence between the curves and the number of branches per chain. (b) End-to-end vector orientational correlation function, where $\langle\cos\theta_t\rangle = (1/M)\sum_{i=1}^{M}\langle(\mathbf{v}_{i;t_0}\cdot\mathbf{v}_{i;t_0+t})/(|\mathbf{v}_{i;t_0}||\mathbf{v}_{i;t_0+t}|)\rangle$ is the cosine of the angle between the vector spanning the first and last monomers between time t_0 and time t_0+t averaged over all chains in the simulation box and all initial times t_0 in the time series.

Fig. 3(a) shows $\langle R^2(s)\rangle/(sl_{CG}^2)$ for the initial linear system alongside its branched counterparts. All systems collapse strongly, indicating that the insertion of (short) branches does not cause any significant change of conformations and that all production simulations are

well equilibrated. Such a negligible perturbation by the branches is expected as evidenced by melt studies which vary the branch content in a larger range.[51] The solid (black) line presents the theoretical prediction from the freely-rotating chain (FRC) model[52,53] which may be defined as

$$\langle R^2(s)\rangle = s\langle l_{\mathrm{CG}}^2\rangle\left(\frac{1+\alpha}{1-\alpha} - \frac{2}{s}\,\frac{\alpha(1-\alpha^s)}{(1-\alpha)^2}\right) \tag{6}$$

where $\alpha = -\langle\cos\theta\rangle$ and θ is the bond angle as before. The value of $\langle\cos\theta\rangle$ for the united-monomer model may be found via direct integration of the tabulated angular potential U_{angle}, as depicted in Fig. 1, via

$$\langle\cos\theta\rangle = \frac{\int_0^\pi \mathrm{d}\theta\ \sin\theta\cos\theta\exp\left(-\beta U_{\mathrm{angle}}(\theta)\right)}{\int_0^\pi \mathrm{d}\theta\ \sin\theta\exp\left(-\beta U_{\mathrm{angle}}(\theta)\right)} \tag{7}$$

where $\beta = 1/k_{\mathrm{B}}T$. Alternatively, one may also evaluate the intra-chain bond-bond orientational correlation function directly from simulations $\alpha \equiv \langle\mathbf{b}_{i,j}\cdot\mathbf{b}_{i,j+1}\rangle/\langle l_{\mathrm{CG}}^2\rangle$ where $\mathbf{b}_{i,j}$ is the j-th bond vector of the i-th chain. Both methods yield identical results. It is noteworthy that a small increase is observed with increasing SCB content, $\alpha = 0.7003, 0.7005, 0.7009$, 0.7014, 0.7031 and 0.7062 for $N_{\mathrm{b}} = 0$, 1, 2, 4, 10 and 20 SCBs per chain, implying a weak increase of the average bond angle with increasing SCB content. Concerning the FRC model fit in Fig. 3(a), the α value found for the linear system is used in Eqn. (6) which provides a lower bound, slightly underestimating the internal distances at large ($s > 10$) values. The value of characteristic ratio for the CG-PE model (denoted by $C_{\infty_{\mathrm{CG}}}$ in the following) also agrees well the experimental results (denoted by C_∞ in the following) after remapping using the following relationship,

$$C_\infty = C_{\infty_{\mathrm{CG}}}\frac{\langle l_{\mathrm{CG}}^2\rangle}{\lambda\langle l_{\mathrm{CH}}^2\rangle} \tag{8}$$

where $\lambda = 2$ for two CH_2 monomers per CG bead in the united-monomer model. For this

model $C_{\infty_{\mathrm{CG}}} \approx 5.673$ and when remapped to an atomistic level, $\langle l^2_{\mathrm{CG}} \rangle / (\lambda \langle l^2_{\mathrm{CH}} \rangle) \approx 1.318$, corresponds to $C_\infty = 7.476$ which is in excellent agreement with experimental studies.[25,54] The characteristic triple-well bending potential is clearly advantageous and provides the additional rigidity necessary to ensure the chain stiffness lies within the acceptable range of experimental values. Other models (i.e. with single-well potentials) have been known to underestimate the persistence length of PE, as detailed by Hall *et al.*[25]

By utilising the method outlined in the previous section, it may be demonstrated that the introduction of SCBs does not significantly disturb the starting topology. In this way, the entanglements initially present in the melt are then preserved and as a result all metrics, commonly used to characterise well equlibrated systems of polymers, appear mostly unaltered. This is indicated in Fig. 3 by the strong overlap between all systems not only for static properties, such as the MSID but also for dynamic properties, such as the time-dependent end-to-end vector correlation function. It is well known that the relaxation time for entangled polymer melts increases with increasing molecular weight of the chains. This presents a serious bottleneck in simulations of very long polymers. For example, the relaxation time for a monodisperse melt comprising chains of length N scales as $N^{\approx 3.4}$ due to entanglements, which translates to approximately $N^{\approx 4.4}$ in cpu time.[48] Numerous different methods have been devised to overcome this slowdown with N, including push-off algorithms[48] or connectivity-altering Monte Carlo moves.[48,55] These methods for monodisperse chains, followed by the aforementioned techniques to insert SCBs, provide access to very large systems with longer chains where relaxation times are long and computational resources are scarce. The method used here shows only a single long production simulation need be performed, with several shorter post-production runs required after the introduction of SCBs. In combination these methods may pave the way for the study of high-molecular weight systems, likely with long-chain branches that are several hundreds of carbons long. The study of the latter system, obtained here still by conventional MD, will be the subject of a forthcoming article. The remainder of this article now focuses on the thermodynamic and structural

properties of these systems with and without SCBs on cooling and heating.

Melting and Crystallisation

In order to probe the influence of SCBs on the crystallisation and melting behaviour of PE, each of the systems considered (with N_b = 0, 1, 2, 4, 10 and 20 SCBs per chain) have been subjected to a series of cooling and heating cycles from T = 227°C (T = 1.0) to T = −23°C (T = 0.5) at four different rates 4 K/ns, 1 K/ns, 0.1 K/ns and 0.04 K/ns from fastest to slowest respectively, covering more than two decades. The slowest rate of 0.04 K/ns is bifurcated from the 1.0 K/ns rate at T = 152 °C for computational expedience. In anticipation that SCBs strongly influence the domain size in the final crystal structure, the systems with $N_\mathrm{b} > 1$ were doubled in size to ensure the influence of finite box size is less strongly felt and justifiable comparisons made between the systems with different N_b. Smaller systems were initially considered comprising approximately 20,000 particles. However, the finite box size drastically limited the domain size obscuring the influence of SCBs, see for example SI Fig. S1 for the stem length distributions of these systems.

Observing Fig. 4 from left to right shows that slower cooling leads to a larger density jump as the hysteresis cycle becomes much higher, and the peak of the heat capacity becomes more pronounced (second row). For the highest branch content, however, the hysteresis loop remains very small, indicating extremely poor crystallization even at the slowest cooling rate. The crystallization and melting temperatures obtained from the peak positions in the heat capacity are reported in Fig. 5 either as a function of cooling rate or branch content.

Going into more detail, Fig. 4(a) shows the effect of the fastest cooling rate (4 K/ns) on the density-temperature profiles of each of the different systems considered. It is apparent that, due to rapid cooling, the crystallisation is very poor and this is reflected in the non-monotonicity of the crystallisation temperature T_c (Fig. 5(b) green curve) and low final density after the systems have crystallised which decreases slightly with increasing branch

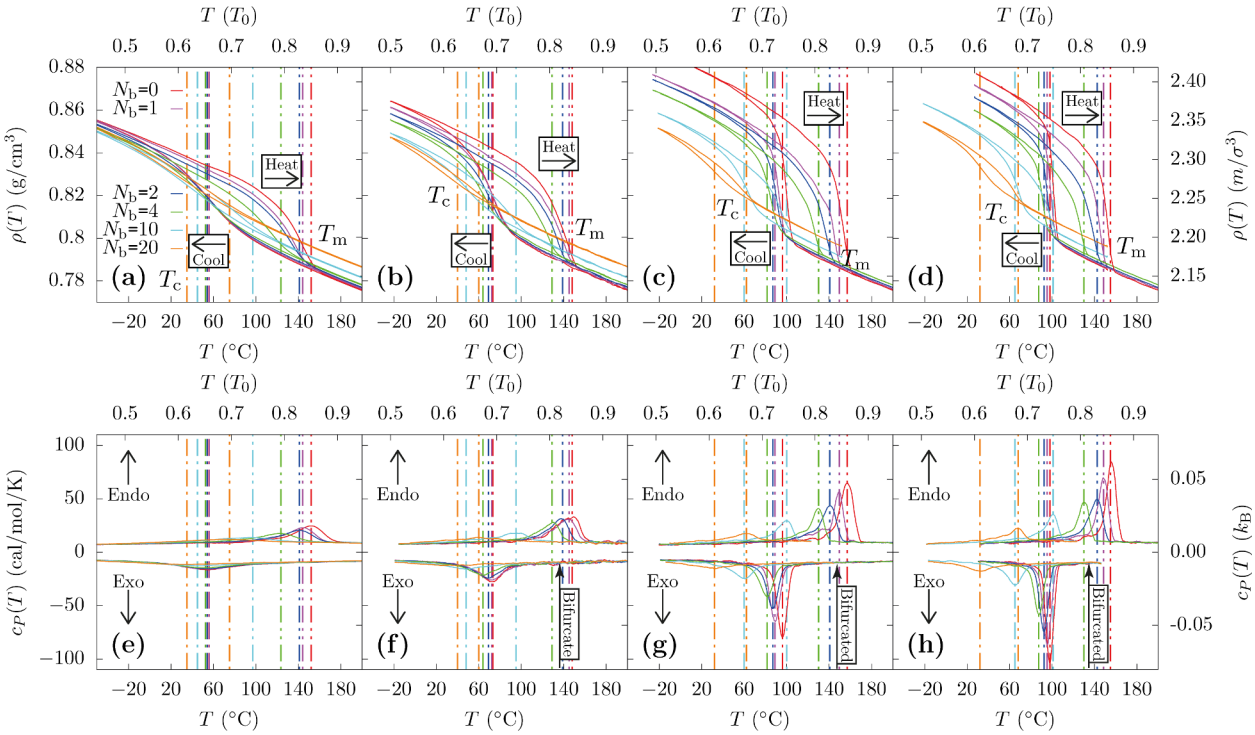

Figure 4: Crystallisation and melting of PE melts. (a-d) Density-temperature trace for all systems with $N_b = 0$, 1, 2, 4, 10 and 20 SCBs per chain (red, pink, blue, green, cyan, orange) subjected to cooling and heating cycles for each of the different rates considered 4 K/ns, 1 K/ns, 0.1 K/ns and 0.04 K/ns (from left to right indicates slower cooling). The crystallisation and melt temperatures (T_c and T_m respectively) are indicated in each figure by dashed lines along with the cooling and heating directions for each set of curves. Note all curves in panels (d,h) and curves corresponding to $N_b = 10$ and 20 in panels (c,h) are obtained by bifurcating from the systems in panels (b,f) for computational expedience at $T = 152$°C, i.e. cooling at 1 K/ns to $T = 152$°C and switching to the slower rates of 0.1 K/ns and 0.04 K/ns for the remainder. (d-f) Specific heat (at constant pressure c_P) exotherms and endotherms on cooling and heating respectively as indicated by the arrows. This is obtained by taking the derivative of the enthalpy ($H = U + PV$) w.r.t temperature ($\mathrm{d}H/\mathrm{d}T)_P$. The endo and exo curves have been shifted for clarity. Note the strong monotonic increase in peak height at both T_c and T_m as the cooling/heating rates are decreased, indicating an improved crystalline morphology. Note also the monotonic decrease in peak height with an increasing number of branches, implying a worsening of the crystalline morphology.

number. This would suggest chains are less cleanly packed in systems with a large number of branches. (Note the glassy appearance of the final crystalline structure, see SI Fig. S2.). While the results in Fig. 5 for different SCB content are similar at each cooling rate, on subsequent heating, there is a noticeable dependence of the results on SCB content, with the melt temperatures T_{m} differing even with rapid heating (Fig 5 (a)). An even greater difference is then observed between systems upon slower heating, see Fig 5 (b,c) and (d). This is likely the combined effect of smaller crystals in the branched systems but also exacerbated by the fast heating rate which overestimates the melt temperature[15,25] and the periodic boundary which enhances the stability of the crystalline domains. The observed hysteresis behaviour is also characteristic of first-order phase transitions. In classical nucleation theory, there is competition between the bulk free energy gain of the new phase and energetic costs associated with the formation of new (crystal-melt) interfaces, known as a nucleation barrier. Only once a nucleus becomes large enough can it overcome the barrier and grow stably. At large undercoolings this barrier is smaller and along with it the critical nucleus size thus nucleation density is high. The larger difference between T_{c} and T_{m} is therefore attributed to what is considered a 'deep-quench' on experimental timescales and finite box size which stabilises the crystalline domains through the periodic boundary.[18]

As the cooling rate is decreased, Fig. 4(b-c) shows that all systems further separate and T_{c} is raised for all systems except for the system with the highest branch content. With slower cooling, there is more time for the chains to rearrange and for structures to form. This improves the final crystalline structure and explains why all systems crystallise at higher temperatures. A systematic decrease of T_{c} with SCB content is also apparent which indicates SCBs shift crystallisation to lower temperatures (Fig. 5(b)). The reason for this is not immediately apparent due to the fast cooling rate and poor crystallisation. A possible explanation is that branches prevent the chains from attaching to the crystallites so that stronger undercooling is required to trigger crystallisation. Furthermore a longer time is required for chains with branches to rearrange and fold into the correct conformation to

join a growing crystal domain. Even with slower cooling there is insufficient time for this rearrangement to occur, leading to a glassy looking structure. The final density between all systems after crystallisation reflects this and also decreases as the number of branches is increased. No clear trend appears in the final melt temperature with a decreasing heating rate as shown most clearly in Fig. 5(c). This is likely due to a number of factors. The kinetic pathway to the best crystalline structure may become blocked in systems with branches, due to fast cooling and slow dynamics of chain rearrangement, which leads to poor crystals and lowers the melt temperature, consequently enhancing the difference in melt temperature between systems. In addition, the rapid heating rate is known to overestimate the melt temperature in simulation as discussed previously, due to the stabilisation of crystalline domains through the periodic boundary.

For the slowest rate (0.04 K/ns), which is a factor 100 slower than the fastest rate considered in this work, the crystallisation temperatures are raised dramatically by almost 50°C in some cases as shown in Fig. 4(d) and Fig. 5(d) compared to the fastest rate in Fig. 4(a). At a given rate, the crystallisation temperature varies little up to one branch per 100 carbons ($N_\mathrm{b} = 1$) where T_c is lowered by 15°C with respect to the equivalent without SCBs. At higher SCB content, the crystallisation temperature becomes significantly lower, and the variation with rate is less pronounced. At one branch per 20 carbons ($N_\mathrm{b} = 20$), there is no effect of cooling rate on the transition within the precision of the simulations and the crystallinity is extremely poor as illustrated in Fig. 6(f). The final density and peak depth in the specific heat exotherm which are both significantly larger for the system without branches when compared to those with high SCB content are highly suggestive of a modified crystalline structure and smaller domain size in the branched systems. The SCBs almost never crystallise and when there are only very few branches, the crystalline part of the lamella structure can appear almost completely unaltered. In this scenario the branches are simply forced out into the amorphous region hence the overall density is lower but does not necessarily reflect a poorer crystal or smaller domain size. On heating, the melt

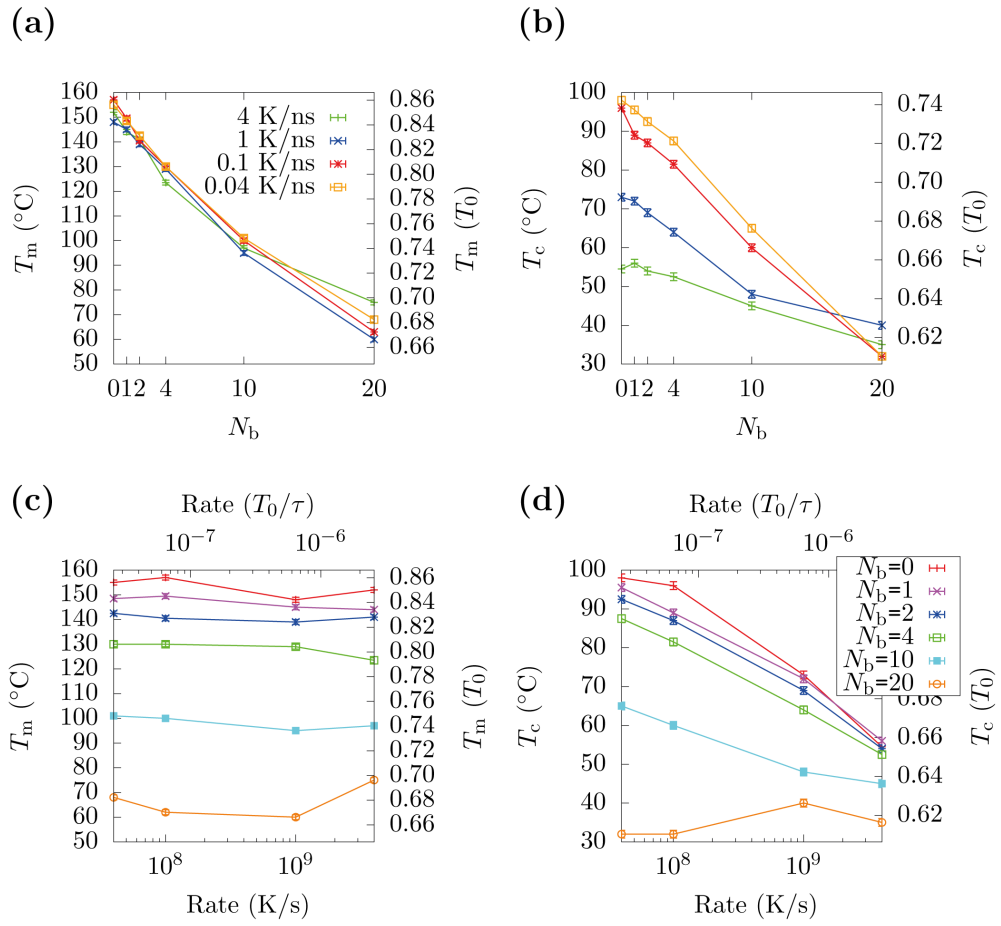

Figure 5: Trends of system observables with cooling rate and branch content. (a,b) Melt temperature and crystallisation temperature vs increasing branch number for all rates considered. Note the systematic decrease in T_c with increasing branch number. The key in panel (a) is the same for panel (b). (c,d) Melt temperature and crystallisation temperature vs rate for each system with differing numbers of branches. Note the systematic decrease in T_c with faster cooling. The key in panel (d) is the same for (c).

temperature for the branched systems are all comparable. However, the linear system melts nearly 10°C above the system with only a single SCB per chain. The raised T_{m} and high density is indicative of larger crystalline domains. Note that the melt temperature is still an overestimate for extended C400 alkanes, which is around 140°C,[56] caused by the high heating rates employed in the simulation compared to experiments.

In order to understand the influence of SCB on the crystalline morphology in more detail, the distribution of stem lengths inside the crystallites are compared for the different systems. This is achieved by traversing along the backbone of all chains, excluding SCBs, and identifying stems with successive bond angles within a predefined interval $145^\circ \leq \theta \leq 180^\circ$. This interval corresponds to the width of the trans-trans minimum in the angular potential, see Fig. 1. Figure 6 shows the stem length distributions for each of the systems at the end of their respective cooling runs alongside the corresponding snapshots (a-f). The colour correspondence between snapshots, chain architecture and stem length distributions are indicated by the inset model chains. For each distribution a Gaussian fit is performed for all stems with length larger than 10 $\sigma/2$, to exclude the amorphous region and the peak position is taken as the average stem length.

Figure 6(a) shows the stem length distribution of the linear system, where the light to dark curves indicate slower cooling. As the cooling rate is decreased the crystalline peak height moves to longer stem lengths and the amorphous peak height is reduced, reflecting a shift of amorphous beads into the crystalline region and an improved crystalline structure and large crystals. This is neatly summarised by the (red) curve in Fig. 7(c) which shows the average stem length (peak position) increases with a decreasing cooling rate and is consistent with the T_{c} dependence on cooling rate in Fig. 5(b,d) and final density in Fig. 4. The rate dependence of stem length is apparent for all systems considered but the branched systems clearly deviate more strongly from the linear system and speculatively tend towards a plateau. This is most apparent for the $N_{\mathrm{b}} = 4$ system which has strongly overlapping stem length distributions and identical average stem lengths, after cooling at 0.1 K/ns and

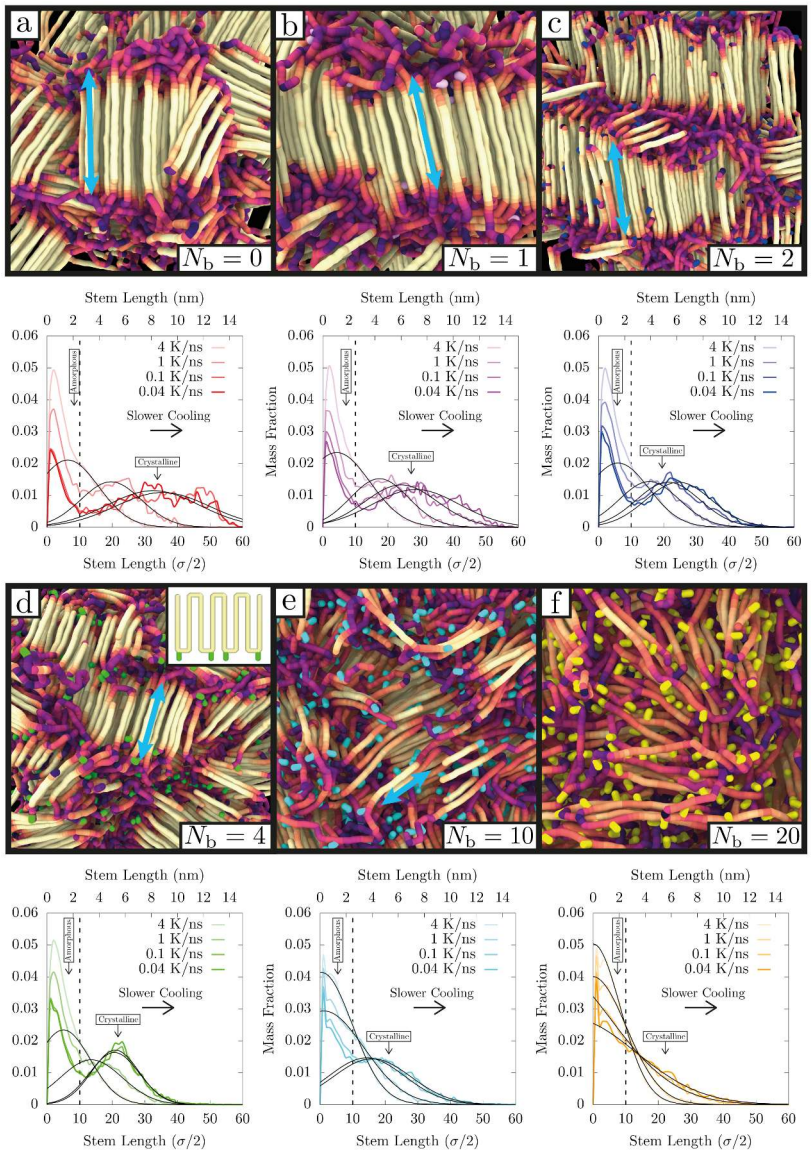

Figure 6: Structural properties in the crystalline phase. (a-f) Snapshots from MD simulations of the crystalline structure for each of the systems considered with N_b = 0, 1, 2, 4, 10 and 20 SCBs per chain respectively from the end of the slowest cooling simulations 0.04 K/ns, produced using OVITO.[57] Backbone bonds are coloured continuously, according to their local P_2 order parameter, from yellow (P_2=1) to purple (P_2=-0.5). Chain branches are highlighted in pink, blue, green, cyan and orange for the systems with N_b = 1, 2, 4, 10 and 20 SCBs per chain respectively. The inset arrows are an indication of the maximum attainable stem length which decreases with increasing SCB content and the 'tetris-like' schematics are representative of the changing molecular architecture between successive snapshots. The corresponding stem length distributions for the snapshots as a mass fraction of the total system size, at the end of the respective cooling runs, are shown below for all cooling rates considered. The dashed line separates the regions of the stem length distribution which correspond approximately to the amorphous and crystalline regions as indicated by the inset labels. Darker curves indicate slower cooling and the black lines are a gaussian fit of the data above a predefined cutoff at 10 (σ/2), the inset in panel (d) is an illustration of the once-fold-twice-branch structure occurring in the N_b = 4 system which serves to limit the maximum attainable stem length. Note the strong overlap of the two slowest cooling rates in panel (d).

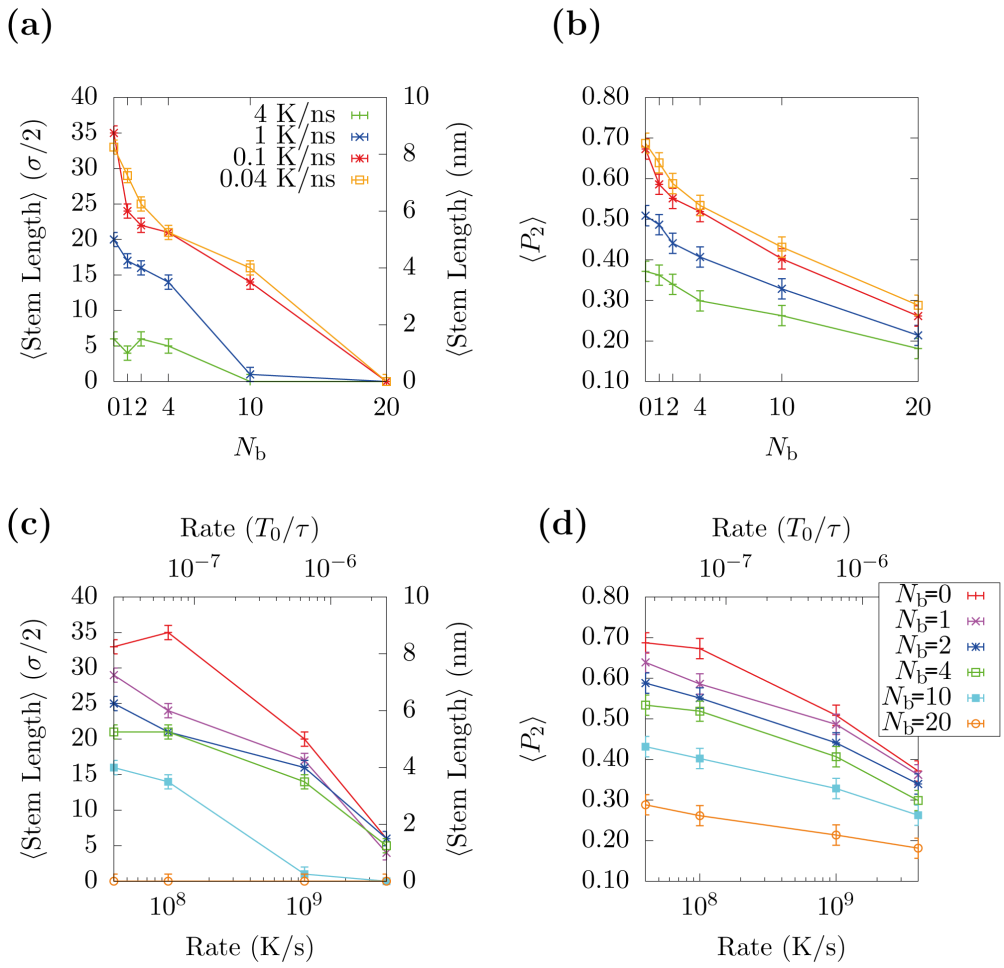

Figure 7: Trends of system observables with cooling rate and branch content. (a,b) Average stem length and local nematic order parameter vs increasing branch number for all rates considered. Note the systematic decrease in stem length and local crystallinity with increasing branch number. The key in panel (a) is the same for panel (b). (c,d) Average stem length and local nematic order parameter vs rate for each system with differing numbers of branches. Note the systematic decrease in stem length and local crystallinity with faster cooling. The key in panel (c) is the same for panels (d). All measurements are taken at room temperature $T = 0.6T_0$ ($\sim 27°$C) to ensure a fair comparison between systems.

0.04 K/ns. At the highest examined branch content, the stem length distribution does not exhibit a peak beyond 10 bonds, making it impossible to define a stem length. The snapshot in Fig. 6(f) shows no light yellow regions, indicating the absence of local crystalline order and is instead replaced by a vague nematic-like orientation. The orange colour indicates the local alignment of the chain backbones with their neighbours is poorer than in the crystallites but not completely disordered as in the purple amorphous regions.

The systems with more than one branch consistently have a smaller average stem length than their linear counterpart. Only with the fastest cooling rate does the system with a single branch show a similar crystalline structure to the linear system; note the similarity between curves in Figs. 6(a) and (b) for the fastest cooling rate. As the cooling rate is reduced all systems separate and average stem lengths increase, with the branched systems moving away from the linear system as reflected by the peak shift in Figs. 6(c-e). Crucially this deviates more strongly when compared to the unbranched system, suggesting that it is not only the cooling rate that changes stem length but also the SCB content. This is further confirmed on examination of the simulation snapshots at the end of the respective cooling runs as shown in Fig. 6 above each stem length distribution. The SCBs are seen to be forced out of the crystallites into the amorphous region. This limits the stem length and reduces the domain size, consistent with observations from previous simulation studies[32] where randomly placed SCBs are seen to cluster in the amorphous regions of the crystalline lamellae. For $N_{\mathrm{b}} = 20$, the large number of branches leaves the remaining linear part of the backbone unable to form locally ordered crystalline regions, allowing for only an approximate nematic orientation to be adopted.

If given sufficiently slow cooling, SCBs will provide control over stem length and ultimately lamella thickness. The $N_{\mathrm{b}} = 4$ system under slow cooling is likely close to this limit since the peak position in Fig. 6(d) corresponds to approximately 25 CG-monomers, which is equivalent to on average one fold between successive branches along the chain backbone. This structure is illustrated by the cartoon panel in Fig. 6(d) and is necessary in order to

force out both the chain ends and SCBs from the crystallites; in some respects the chain ends and SCBs may be thought of as equivalent during crystallisation. It is therefore expected that the stem length dependence on cooling rate will reach a plateau, with even slower cooling and regular branching, equal to half the distance between successive branches (i.e. average stem length $L_{\mathrm{stem}} = N/(2N_{\mathrm{b}})$).

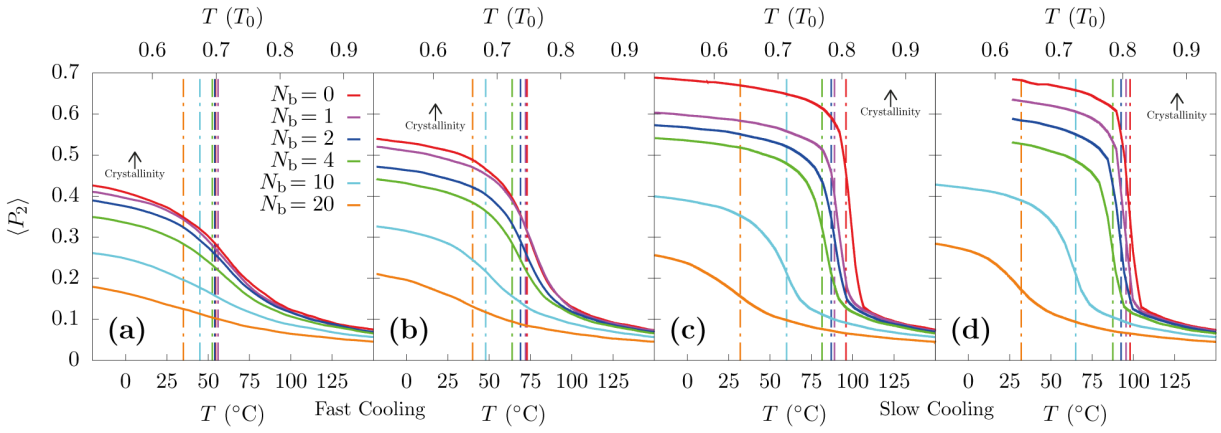

Figure 8: Average crystallinity measured by the local nematic order parameter $P_2 = \langle 3/2\cos^2\theta - 1/2\rangle$ vs temperature on cooling. Rates 4 K/ns, 1 K/ns, 0.1 K/ns and 0.04 K/ns correspond to figures (a), (b), (c) and (d) respectively. The inset arrows indicate increasing crystallinity with decreasing cooling rate. For reference $\langle P_2\rangle = 1$ reflects a perfect crystal and $\langle P_2\rangle = 0$ a completely isotropic liquid, for details of how this calculation is performed see SI. The color code for the number of branches is identical to that used in Fig. 7d.

Evaluating the overall crystallinity of each system requires a suitably defined order parameter. Previous studies of PE have employed the second Legendre polynomial,[11,16,25,43,58,59] defined as $P_2 = (3\langle\cos^2\theta_{i,j}\rangle - 1)/2$ where $\theta_{i,j}$ is the angle between the backbone of two given CG beads and the angular brackets indicate averaging over all beads within a predefined cutoff distance r_{c}, for details see Supporting Information. The second minimum of the radial distribution function is used as the cutoff distance ($\sim 1.6\sigma$) corresponding to the next next nearest neighbour, see Fig. S3. This ensures a local measure of crystallinity which is then averaged at 0.27 ps intervals as each system is cooled.

Figure 8 shows the evolution of crystallinity as each system is cooled with a progressively slower rate. For the fastest cooling rate Fig. 8(a), local ordering is very low, between 0.35

and 0.4 at $T = 0°\mathrm{C}$, consistent with the glassy structure in Fig. S2. This is primarily due to the rapid cooling which allows only a short time for structure formation before the system is effectively frozen in. A larger SCB content further disorders the crystalline structure, likely because the amorphous regions between crystallites must become larger to accommodate the SCBs and because the SCBs cannot crystallise. This explains why the $N_\mathrm{b} = 0$ and $N_\mathrm{b} = 1$ systems have identical average stem lengths but the $N_\mathrm{b} = 1$ has both slightly lower density and crystallinity. Hence the lower crystallinity cannot be attributed entirely to the reduced domain size but also the mass fraction of SCB content. As the cooling rate decreases, Figs. 8(b-d) show that the crystallinity increases with both decreasing SCB content and decreasing cooling rate, as qualitatively expected and in accord with the behavior of the density curves shown in Fig. 4.

The difference between the final crystal structures is also revealed by the static structure factor $S(q)$ which allows a direct comparison with experiment. The structure factor is defined as

$$S(q) = \frac{1}{M_\mathrm{tot}} \left\langle \sum_{i,j=1}^{M_\mathrm{tot}} \mathrm{e}^{\mathrm{i}\mathbf{q}\cdot(\mathbf{r}_i - \mathbf{r}_j)} \right\rangle_{|\mathbf{q}|=q\pm dq} \tag{9}$$

where the sum is performed over all monomers $M_\mathrm{tot} = MN$ in the system (with M chains and N monomers per chain) and the angular brackets indicate averaging over all q-vectors of length $q \pm dq$. A running average is applied in the interval $q_r = \pi/L_\mathrm{box}$ with bin size $0.01\sigma^{-1}$. Since only q-vectors compatible with the finite box size may be considered, the precision becomes increasingly poor as $S(q)$ approaches the box size.[18]

After crystallisation, the structure factor, Fig. 9, develops sharp peaks at high q (WAXS range) and a broad hump at low q (SAXS range). The small-q peak corresponds to the size of crystalline domains. The higher the branch content, the less pronounced is this peak. For the highest branch content $N_\mathrm{b} = 20$ it is almost absent, and there are no peaks at high q either, quantifying the absence of crystallinity.

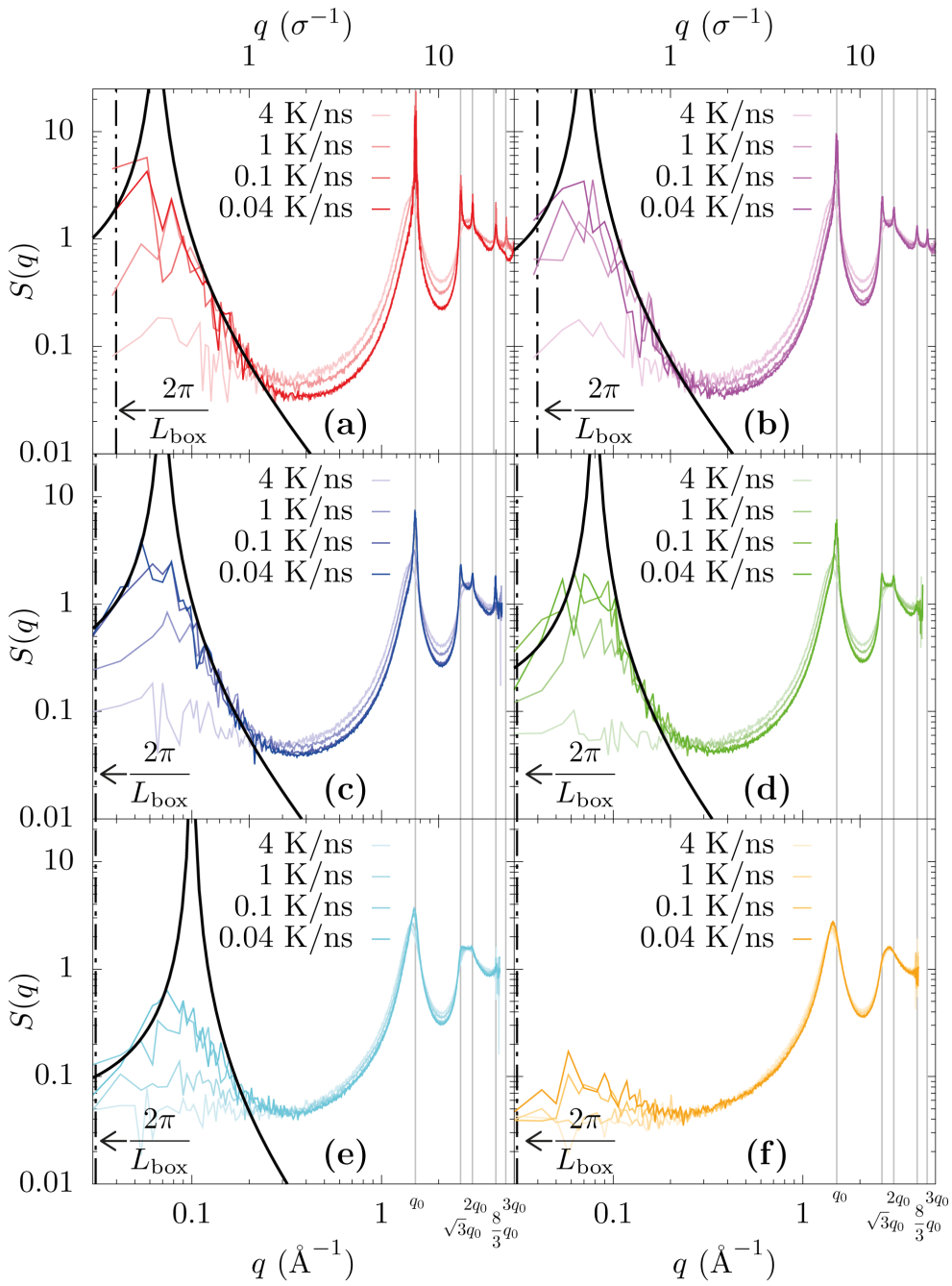

Figure 9: Total structure factor $S(q)$ in the crystalline phase at room temperature $T = 0.6T_0$ ($\sim$ 27°C). Panels (a-f) correspond to the systems with $N_\mathrm{b} = 0, 1, 2, 4, 10$ and 20 branches respectively. Darker curves indicate slower cooling as indicated by the key in each panel. The simulation box size ($2\pi/L_\mathrm{box}$) is indicated by the arrows and dashed lines. Note the branched systems $N_\mathrm{b} \geq 2$ contain double the number of chains of its linear counterpart, hence allow to start at slightly smaller q-vectors. The sharp peaks of the (2d) hexagonal lattice are strongest for the systems without branches after slow cooling, q_0 corresponds to 1.506 Å^{-1}. The black solid lines correspond to a Lorentzian fit of the low-q envelope where $L(q) = \frac{1}{\pi}\frac{\frac{1}{2}\Gamma}{(q-q_0)^2+(\frac{1}{2}\Gamma)^2}$, Γ and q_0 correspond to the peak width and peak position respectively.

Figure 9 reveals the stark contrast between the $N_b = 4$ system cooled fast (d) and the $N_b = 0$ system cooled slowly (a). The sharp Bragg peaks for the $N_b = 0$ system are characteristic of the (2d) hexagonal lattice structure, i.e. they occur at $(1 : \sqrt{3} : 2)$ times the q-value of the first sharp peak at $q_0 = 1.506$ Å^{-1}, indicating a good crystallinity and large structure formation at low q-values. For the highly branched system ($N_b = 4$) and fast cooling, $S(q)$ has less pronounced peaks for $q > q_0$ and only increases weakly as q tends to 0. This is indicative of only weak local order and relatively small crystalline domains, in agreement with the discussion above. To illuminate the physics otherwise lost in the low-q region, a Lorentzian fit is performed on the envelope of the low-q peak i.e. a fitting of the upturn and downturn of the peak. In this way it is possible to approximate the q-value of the peak position. The approximate positions correspond to $q = 0.065$, 0.065, 0.069, 0.080 and 0.01 for $N_b = 0, 1, 2, 4$ and 10 respectively. This corresponds to a lamella spacing of 9.7 nm, 9.7 nm, 9.3 nm, 7.5 nm and 6.3 nm. These values are slightly larger ($\pm 1nm$) than the average stem length in Fig 7 (a) (0.04 K/ns) however this is likely due to the assumptions made during the stem length analysis, the contribution to the structure factor from the amorphous region and the approximate fitting to noisy data. It is clear however that the inward shift of the low-q region with increasing SCB content is a result of the reduced domain size and smaller lamella spacing.

Conclusions

Studying the crystallisation behaviour of PE and ultimately the origin of specific structural characteristics, i.e. flexibility, fracture toughness, puncture resistance, etc., requires understanding in detail the crystalline morphology. These different properties arise due to subtle differences in chain architecture or system composition, such as branch content and molecular weight distribution. Simulations provide clean systems where structure-property relationships like these may be tested precisely. However, owing to the long chain lengths and large

lamellar structures present in real polymers, it is a necessity that systems be large enough to study multi-domain structures. Furthermore, the subtle differences between systems and sheer number of parameters present a dauntingly large ensemble of systems to choose from, each of which must be equilibrated in the same way with long chains and consequently long run-times which is a serious bottleneck.

Here the issue of system size was reduced by coarse-graining out structural details on local length scales (using the united-monomer model) which are expect not to be crucial for the formation of large scale structures during polymer crystallisation. In addition the subtle difference between systems was turned to our advantage by instead growing different branched architectures into the linear melt and performing a short post-production relaxation, instead of a longer relaxation of each system individually starting from a random walk and subsequent slow push-off of excluded volume. This was demonstrated to be a viable method and was reflected most prominently in the characteristic observables used to identify well equilibrated polymer melts, which remained essentially unaltered after growth of the branches. Our method is ideally suited to systems comprising a small number of short branches, not unlike industrial PE samples. However when the number of branches is large, i.e. in the case of bottle-brush polymers, a substantial modification relative to the linear chain structure should be expected.

In this study, we concentrated on chains with few branches as is typical of LLDPE. We observe that going beyond one branch per 100 carbons leads to extremely poor crystallisation. For one branch per 20 carbons, crystalline order was effectively suppressed. When studying the influence of regularly spaced SCBs and cooling rate on the structural properties of PE crystals, it was shown that lamellar thickness strongly depends on both quantities. In particular the domain size decreases with faster cooling and increasing SCB content. Slower cooling allows longer times for chains to rearrange and attach to the crystal growth front, leading to larger structures, and SCBs limit the maximum attainable stem length scale due to the required rejection of SCBs and chain ends from crystallites. This was seen most

clearly in the $N_b = 4$ system where the stem length speculatively reaches a plateau with slower cooling, owing to the $2M$ chain ends which must be accommodated.

In comparison to linear PE melts, there are still relatively few simulation studies of PE with SCBs included.[4,14,24,31–35] Many of these studies considered all atom systems composed of short chains (C_{50}),[14] which are too small to form chain folded structures, or system sizes comprising only one or two long chains.[31,36,37] However all studies agree that SCBs are strictly excluded from the crystallites and rejected into the amorphous regions (with the exception of methyl and ethyl which can, at least partially, crystallise[14] in short chain systems) and indeed that chains have a tendency to fold at branch point in order to facilitate rejection. One recent study considered the effect of 3 randomly spaced SCBs along the backbone of long $C_{1292}H_{2586}$ chains mixed with $C_{320}H_{642}$ at varying molecular weight fractions, employing a CG modelling strategy similar to ours.[32] In keeping with their findings we also note that crystallinity is reduced with increasing SCB content and that there is a lower limit of crystal thickness due to SCB content. However due to the random placement of the SCBs it is difficult to compare the dependence of lamella thickness on SCB content. Regular and randomly placed SCB distributions are quite different. We expect 3 regularly spaced branches on $C_{1292}H_{2586}$ to be comparable to our $C_{400}H_{802}$ system with a single SCB placed in the center. This yields approximately the same distance between the chain ends and the first SCB along the backbone which we demonstrate controls lamella thickness. Stem lengths reported in the aforementioned study[32] under similar cooling conditions (0.2 K/ns) are around 14 beads (UL100). This differs considerably when compared to the average stem lengths reported in this work of around 25-30 beads under similar cooling conditions (Figs. 6(f) and 7(a)). We conclude this difference in stem lengths is most likely due to the random placement of the SCBs which destroy the regularity of the lamella spacing seen here and the faster cooling rates employed.

The systems studied in this work provide a proof of concept of how branched PE systems may be studied with relatively small computational expense in comparison to their linear

counterparts. In this way, larger systems may be studied with longer chains, several hundreds of carbons long and multiple branched architectures grown into them starting from only a single production simulation.

Building on the results presented here, it will be interesting to investigate the effects of bidispersity and molecular weight distribution on the crystallisation behaviour of systems containing SCBs, both of which are of interest to the industrial community and known to improve material flexibility. Furthermore the branch distribution and indeed the regularity of the branches along the backbone may be altered to reflect the accuracy of certain catalysts or indeed polymerisation steps. Work in these directions is currently underway.

Acknowledgement

W.S.F., J.B. and H.M. acknowledge funding support from TotalEnergies via grant IPA–6352. The authors would like to acknowledge Dr Olivier Benzerara for technical support and Dr Kamila Kazmierczak for administering the project. We thank the High Performance Computing Center CAIUS of the University of Strasbourg for supporting this work by providing access to computing resources, partly funded by the Equipex Equip@Meso project (Programme Investissements d'Avenir) and the CPER Alsacalcul/Big Data. A generous grant of computer time at the national computer center GENCI/IDRIS is also gratefully acknowledged (grant no A0110913034).

Supporting Information Available

Stem length distributions for the systems comprising approximately 20,000 particles. Additional snapshots for the $N_\mathrm{b} = 0$ and $N_\mathrm{b} = 4$ cooled at 4 K/ns. Sample LAMMPS script for growing branches. Radial distribution function and details of the P_2 order parameter calculation. Details of all atom simulations.

References

(1) Ungar, G.; Zeng, X.-b. Learning polymer crystallization with the aid of linear, branched and cyclic model compounds. *Chemical Reviews* **2001**, *101*, 4157–4188.

(2) Ramos, J.; Vega, J.; Martinez-Salazar, J. Predicting experimental results for polyethylene by computer simulations. *European Polymer Journal* **2018**, *99*, 298–331.

(3) Luo, C.; Sommer, J.-U. Frozen Topology: Entanglements Control Nucleation and Crystallization in Polymers. *Phys. Rev. Lett.* **2014**, *112*, 195702.

(4) Kumar, V.; Locker, C. R.; in't Veld, P. J.; Rutledge, G. C. Effect of short chain branching on the interlamellar structure of semicrystalline polyethylene. *Macromolecules* **2017**, *50*, 1206–1214.

(5) Rojas, G.; Inci, B.; Wei, Y.; Wagener, K. B. Precision polyethylene: Changes in morphology as a function of alkyl branch size. *Journal of the American Chemical Society* **2009**, *131*, 17376–17386.

(6) Ungar, G.; Zeng, X.; Brooke, G. M.; Mohammed, S. Structure and formation of non-integer and integer folded-chain crystals of linear and branched monodisperse ethylene oligomers. *Macromolecules* **1998**, *31*, 1875–1879.

(7) Brooke, G. M.; Burnett, S.; Mohammed, S.; Proctor, D.; Whiting, M. C. A versatile process for the syntheses of very long chain alkanes, functionalised derivatives and some branched chain hydrocarbons. *Journal of the Chemical Society, Perkin Transactions 1* **1996**, 1635–1645.

(8) Hosier, I.; Bassett, D. A comparison of the morphology and crystallization kinetics of two centrally branched monodisperse alkanes with n-alkanes of equal and half length. *Polymer* **2002**, *43*, 5959–5967.

(9) Rastogi, A.; Hobbs, J.; Rastogi, S. Time-resolved WAXD and SAXS investigations on butyl branched alkane at elevated pressures. *Macromolecules* **2002**, *35*, 5861–5868.

(10) Zeng, X.; Xie, F.; Ungar, G. Semicrystalline and superlattice structures in an asymmetrically methyl-branched long-chain alkane. *Macromolecules* **2007**, *40*, 5750–5758.

(11) Zhang, R.; Fall, W. S.; Hall, K. W.; Gehring, G. A.; Zeng, X.; Ungar, G. Quasi-continuous melting of model polymer monolayers prompts reinterpretation of polymer melting. *Nature Communications* **2021**, *12*, 1–7.

(12) Gartner III, T. E.; Jayaraman, A. Modeling and simulations of polymers: a roadmap. *Macromolecules* **2019**, *52*, 755–786.

(13) Tang, X.; Chen, W.; Liangbin, L. The Tough Journey of Polymer Crystallization: Battling with Chain Flexibility and Connectivity. *Macromolecules* **2019**, *52*, 3575–3591.

(14) Zhang, W.; Larson, R. G. Direct all-atom molecular dynamics simulations of the effects of short chain branching on polyethylene oligomer crystal nucleation. *Macromolecules* **2018**, *51*, 4762–4769.

(15) Waheed, N.; Lavine, M.; Rutledge, G. Molecular simulation of crystal growth in n-eicosane. *The Journal of Chemical Physics* **2002**, *116*, 2301–2309.

(16) Yi, P.; Locker, C. R.; Rutledge, G. C. Molecular dynamics simulation of homogeneous crystal nucleation in polyethylene. *Macromolecules* **2013**, *46*, 4723–4733.

(17) Meyer, H.; Müller-Plathe, F. Formation of chain-folded structures in supercooled polymer melts. *The Journal of Chemical Physics* **2001**, *115*, 7807–7810.

(18) Meyer, H.; Müller-Plathe, F. Formation of chain-folded structures in supercooled polymer melts examined by MD simulations. *Macromolecules* **2002**, *35*, 1241–1252.

(19) Reith, D.; Meyer, H.; Müller-Plathe, F. Mapping atomistic to coarse-grained polymer models using automatic simplex optimization to fit structural properties. *Macromolecules* **2001**, *34*, 2335–2345.

(20) Luo, C.; Sommer, J.-U. Disentanglement of linear polymer chains toward unentangled crystals. *ACS Macro Letters* **2013**, *2*, 31–34.

(21) Luo, C.; Sommer, J.-U. Role of thermal history and entanglement related thickness selection in polymer crystallization. *ACS Macro Letters* **2016**, *5*, 30–34.

(22) Jabbari-Farouji, S.; Rottler, J.; Lame, O.; Makke, A.; Perez, M.; Barrat, J.-L. Plastic deformation mechanisms of semicrystalline and amorphous polymers. *ACS Macro Letters* **2015**, *4*, 147–150.

(23) Jabbari-Farouji, S. Static and dynamic scaling behavior of a polymer melt model with triple-well bending potential. *Journal of Polymer Science Part B: Polymer Physics* **2018**, *56*, 1376–1392.

(24) Zhai, Z.; Morthomas, J.; Fusco, C.; Perez, M.; Lame, O. Crystallization and molecular topology of linear semicrystalline polymers: simulation of uni-and bimodal molecular weight distribution systems. *Macromolecules* **2019**, *52*, 4196–4208.

(25) Hall, K. W.; Sirk, T. W.; Klein, M. L.; Shinoda, W. A coarse-grain model for entangled polyethylene melts and polyethylene crystallization. *The Journal of Chemical Physics* **2019**, *150*, 244901.

(26) Guerrault, X.; Rousseau, B.; Farago, J. Dissipative particle dynamics simulations of polymer melts. I. Building potential of mean force for polyethelene and *cis*-polybutadiene. *J. Chem. Phys.* **2004**, *121*, 6538–46.

(27) Salerno, K. M.; Agrawal, A.; Perahia, D.; Grest, G. S. Resolving Dynamic Properties

of Polymers through Coarse-Grained Computational Studies. *Phys. Rev. Lett.* **2016**, *116*, 058302.

(28) Salerno, K. M.; Bernstein, N. Persistence Length, End-to-End Distance, and Structure of Coarse-Grained Polymers. *J. Chem. Theory Comput.* **2018**, *14*, 2219–2229.

(29) Moore, T. C.; Iacovella, C. R.; McCabe, C. Derivation of coarse-graned potentials via multistate iterative Boltzmann inversion. *J. Chem. Phys.* **2014**, *140*, 224104.

(30) Vettorel, T.; Meyer, H. Coarse graining of short polythylene chains for studying polymer crystallization. *Journal of Chemical Theory and Computation* **2006**, *2*, 616–629.

(31) Hu, Y.; Shao, Y.; Liu, Z.; He, X.; Liu, B. Effect of short-chain branching on the tie chains and dynamics of bimodal polyethylene: Molecular dynamics simulation. *European Polymer Journal* **2018**, *103*, 312–321.

(32) Moyassari, A.; Gkourmpis, T.; Hedenqvist, M. S.; Gedde, U. W. Molecular dynamics simulations of short-chain branched bimodal polyethylene: Topological characteristics and mechanical behavior. *Macromolecules* **2019**, *52*, 807–818.

(33) Moyassari, A.; Gkourmpis, T.; Hedenqvist, M. S.; Gedde, U. W. Molecular dynamics simulation of linear polyethylene blends: Effect of molar mass bimodality on topological characteristics and mechanical behavior. *Polymer* **2019**, *161*, 139–150.

(34) Hu, Y.; Shao, Y.; Liu, Z.; He, X.; Liu, B. Dominant Effects of Short-Chain Branching on the Initial Stage of Nucleation and Formation of Tie Chains for Bimodal Polyethylene as Revealed by Molecular Dynamics Simulation. *Polymers* **2019**, *11*, 1840.

(35) Ranganathan, R.; Kumar, V.; Brayton, A. L.; Kroger, M.; Rutledge, G. C. Atomistic modeling of plastic deformation in semicrystalline polyethylene: role of interphase topology, entanglements, and chain dynamics. *Macromolecules* **2020**, *53*, 4605–4617.

(36) Sanmartín, S.; Ramos, J.; Martínez-Salazar, J. Following the crystallization process of polyethylene single chain by molecular dynamics: the role of lateral chain defects. **2012**, *312*, 97–107.

(37) Sanmartín, S.; Ramos, J.; Vega, J. F.; Martínez-Salazar, J. Strong influence of branching on the early stage of nucleation and crystal formation of fast cooled ultralong n-alkanes as revealed by computer simulation. *European Polymer Journal* **2014**, *50*, 190–199.

(38) Zhang, M.; Yuen, F.; Choi, P. Differences in the solid-state structures of single-site and Ziegler- Natta linear low-density polyethylenes as revealed by molecular dynamics simulation. *Macromolecules* **2006**, *39*, 8517–8525.

(39) Meyer, H. In *Polymer Crystallization: Observations, Concepts and Interpretations*; Sommer, J.-U., Reiter, G., Eds.; Lecture Notes in Physics; Springer: Berlin, 2003; Vol. 606; pp 177–195.

(40) Milano, G.; Müller-Plathe, F. Mapping Atomistc Simulations to Mesoscopic Models: A Systematic Coarse-Graining Procedure for Vinyl Polymer Chains. *J. Phys. Chem. B* **2005**, *109*, 18609–19.

(41) Reith, D.; Pütz, M.; Müller-Plathe, F. Deriving Effective Mesoscale Potentials from Atomistic Simulations. *J. Comput. Chem.* **2003**, *24*, 1624–36.

(42) Meyer, H.; Wittmer, J.; Kreer, T.; Beckrich, P.; Johner, A.; Farago, J.; Baschnagel, J. Static Rouse Modes and Related Quantities: Corrections to Chain Ideality in Polymer Melts. *Eur. Phys. J. E* **2008**, *26*, 25.

(43) Plimpton, S. Fast parallel algorithms for short-range molecular dynamics. *Journal of Computational Physics* **1995**, *117*, 1–19.

(44) Thompson, A. P.; Aktulga, H. M.; Berger, R.; Bolintineanu, D. S.; Brown, W. M.; Crozier, P. S.; in't Veld, P. J.; Kohlmeyer, A.; Moore, S. G.; Nguyen, T. D., et al. LAMMPS – a flexible simulation tool for particle-based materials modeling at the atomic, meso, and continuum scales. *Computer Physics Communications* **2022**, *271*, 108171.

(45) De Gennes, P.-G. Reptation of a polymer chain in the presence of fixed obstacles. *The Journal of Chemical Physics* **1971**, *55*, 572–579.

(46) Doi, M.; Edwards, S. F. *The Theory of Polymer Dynamics*; Oxford University Press, 1988.

(47) Rubinstein, M.; Colby, R. H., et al. *Polymer physics*; Oxford university press New York, 2003; Vol. 23.

(48) Auhl, R.; Everaers, R.; Grest, G. S.; Kremer, K.; Plimpton, S. J. Equilibration of long chain polymer melts in computer simulations. *The Journal of Chemical Physics* **2003**, *119*, 12718–12728.

(49) Sliozberg, Y. R.; Andzelm, J. W. Fast protocol for equilibration of entangled and branched polymer chains. *Chemical Physics Letters* **2012**, *523*, 139–143.

(50) Sliozberg, Y. R.; Kröger, M.; Chantawansri, T. L. Fast equilibration protocol for million atom systems of highly entangled linear polyethylene chains. *The Journal of Chemical Physics* **2016**, *144*, 154901.

(51) Ramos, J.; Peristeras, L. D.; Theodorou, D. N. Monte Carlo Simulation of Short Chain Branched Polyolefins in the Molten State. *Macromolecules* **2007**, *40*, 9640–9650.

(52) Flory, P. J. *Statistical Mechanics of Chain Molecules*; Wiley Online Library, 1969.

(53) Honnell, K. G.; Curro, J. G.; Schweizer, K. S. Local structure of semiflexible polymer melts. *Macromolecules* **1990**, *23*, 3496–3505.

(54) Horton, J.; Squires, G.; Boothroyd, A.; Fetters, L.; Rennie, A.; Glinka, C.; Robinson, R. Small-angle neutron scattering from star-branched polymers in the molten state. *Macromolecules* **1989**, *22*, 681–686.

(55) Karayiannis, N. C.; Giannousaki, A. E.; Mavrantzas, V. G.; Theodorou, D. N. Atomistic Monte Carlo simulation of strictly monodisperse long polyethylene melts through a generalized chain bridging algorithm. *The Journal of Chemical Physics* **2002**, *117*, 5465–5479.

(56) Stack, G. M.; Mandelkern, L.; Voigt-Martin, I. G. Crystallization, melting, and morphology of low molecular weight polyethylene fractions. *Macromolecules* **1984**, *17*, 321–331.

(57) Stukowski, A. Visualization and analysis of atomistic simulation data with OVITO–the Open Visualization Tool. *Modelling and simulation in materials science and engineering* **2009**, *18*, 015012.

(58) Zhang, R.; Fall, W. S.; Hall, K. W.; Gehring, G. A.; Zeng, X.; Ungar, G. Roughening Transition and Quasi-continuous Melting of Monolayers of Ultra-long Alkanes: Why Bulk Polymer Melting Is Strongly First-Order. *Macromolecules* **2021**, *54*, 10135–10149.

(59) Yamamoto, T. Molecular dynamics simulation of stretch-induced crystallization in polyethylene: Emergence of fiber structure and molecular network. *Macromolecules* **2019**, *52*, 1695–1706.

Graphical TOC Entry